BNL-229519-2026-JAAM

GRP-COSC-19

Evaluating Ru-RuO2@BN as a Bifunctional Electrocatalyst for the Nitrogen Reduction Reaction and the Hydrogen Evolution Reaction

M. Sharma

To be published in "ACS Applied Energy Materials"

February 2026

Chemistry Department

Brookhaven National Laboratory

U.S. Department of Energy

USDOE Office of Energy Efficiency and Renewable Energy (EERE), Office of Sustainable Transportation. Hydrogen Fuel Cell Technologies Office (HFTO)

DISCLAIMER

Evaluating Ru-RuO$_2$@BN as a Bifunctional Electrocatalyst for the Nitrogen Reduction Reaction and the Hydrogen Evolution Reaction

Mitu Sharma,[1,4] Leela Sotsky,[2] Suji Park,[3] Kotaro Sasaki,[4] Anatoly I. Frenkel,[2,4] Gary Halada,[2] and Stanislaus S. Wong[1,*]

[1]Department of Chemistry, Stony Brook University, Stony Brook, New York 11794-3400, USA

[2]Department of Materials Science and Chemical Engineering, Stony Brook University, Stony Brook, New York 11794-3400, USA

[3]Center for Functional Nanomaterials, Brookhaven National Laboratory, Upton, New York 11973-5000, USA

[4]Chemistry Division, Brookhaven National Laboratory, Upton, New York 11973, USA

*To whom correspondence should be addressed.

E-mail: stanislaus.wong@stonybrook.edu

Keywords: ruthenium oxide, boron nitride, nitrogen reduction reaction, hydrogen evolution, electrocatalysis

Abstract – Electrochemical approaches towards clean energy production have been the focus of significant attention. The nitrogen (N_2) reduction reaction (NRR) and the hydrogen (H_2) evolution reaction (HER) offer a promising method for producing NH_3 and H_2, respectively. Nevertheless, practical obstacles that must be overcome in creating optimal catalysts are the sluggish kinetics and low selectivity of NRR and HER. Herein, we report on the synthesis of a Ru-RuO_2-decorated boron nitride (BN) catalyst that shows excellent activity towards NRR. A rate of NH_3 formation (V_{NH3}) of 16.8 μg h^{-1} mg^{-1} and a corresponding Faradaic efficiency (FE) of 52.9 % were noted at a potential of -0.5 V in 0.1 M HCl. However, the HER activity of Ru-RuO_2@BN was found to be highly suppressed in 0.1 M HCl and did not yield a reasonable overpotential value. Thus, the capability of this material towards NRR suggests its viability as a promising catalyst for clean NH_3 production.

1. Introduction

Ammonia (NH_3) is an important chemical which has found ubiquitous use in industry and agriculture.[1] However, the vast majority of NH_3 tends to be produced using the Haber–Bosch process which gives rise to a relatively large carbon footprint, not only necessitating around 2% of the world's annual energy utilization but also releasing harmful greenhouse gases such as CO_2 in relatively large amounts.[2] The electrocatalytic N_2 reduction reaction (NRR) conducted under acidic conditions has emerged as a promising environmentally-friendly alternative to replace the conventional Haber–Bosch process.[3] Another competing process that occurs during NRR is the hydrogen evolution reaction (HER).[4] Electrocatalytic HER is as equally important as NRR, since hydrogen fuel is considered to be the cleanest renewable energy source and represents the fundamental alternative to fossil fuels for our future energy supply.[5] Hence, viable and reliable hydrogen generation is the key prerequisite to achieving a future hydrogen-based economy. [5]

However, as implied, electrocatalytic NRR is hindered by strong competition from HER which can result in low Faradaic efficiencies (FE) and a low NH_3 yield rate (V_{NH3}).[6] Hence, in general, it is thought that suppressing HER can in fact enhance NRR. Nevertheless, as protons are reactants in the NRR, the direct suppression of HER can correspondingly quash NRR, since the hydrogenation of N_2 is significant for N_2 fixation. Hence, if H activation does not occur, then N_2 cannot combine with the H species to form the desired NH_3.[4] Moreover, from a mechanistic perspective, in NRR, the reaction of gaseous N_2 with protons and electrons can form NH_3, but in reducing environments, the protons convert into H_2 in the presence of electrons rather than reacting with N species to form NH_3 molecules.[4] Overall, this can lead to lower V_{NH3} and FE readings. [6] Therefore, a HER-active catalyst is required to design a highly efficient NRR catalyst. Additionally, in the presence of a proton-rich electrolyte, the protons are mostly expected to be activated rather than the robust triple-bonded N≡N. This observation suggests that if a catalyst cannot activate individual protons, then it will not be able to activate the stronger N≡N bond. Hence, the competition between the NRR and HER needs to be considered, when rationally designing and selecting effective catalysts for electrocatalytic N_2 fixation.[7]

The three most common categories of electrocatalysts, i.e., noble metal-based, non-noble-metal based, and metal-free species developed for either NRR or HER, exhibit relatively low ammonia production rates and Faradaic efficiency (FE) (<1%) values, especially when compared with catalysts normally employed for the industrial production of ammonia.[8] However, transition metal (TM) single-atoms, bimetallic catalysts, and metal oxides comprise either empty or partially filled *d* orbital electronic states, suitable for higher NRR activity. The surface of TMs can activate and weaken the strong N≡N bonds by either accepting the lone-pair electron of N_2 to its empty *d*-orbitals or through back-donation of the electrons from its filled *d*-orbitals to the anti-bonding orbitals of N_2.[8-10] Furthermore, the TM oxide (TMO) electrocatalysts have shown attractive NRR properties, owing to their tunable oxidation states and remarkable chemical stability.[8, 11] The structural and morphological modifications of TMO electrocatalysts with the goals of creating electron-rich metallic centers and concomitant oxygen vacancies could play a vital role in enhancing the activity and selectivity of NRR. Specifically, the oxygen vacancies in the TMO with Lewis acid properties could act as the adsorption sites for N_2 molecules possessing a weak Lewis base character.[12]

Of significance to our current study, Ru denotes a promising choice as a metal catalyst for the synthesis of NH_3.[13] In particular, its topmost position on Skülason's volcano diagram reveals that Ru evinces a significant catalytic activity towards NRR, mainly due to its *d*-electron structure.[13, 14] Based upon previous DFT studies by Skúlason and coworkers, Ru yields a suitable

N_2 adsorption energy for NRR and a substantially lower overpotential in dissociative and associative mechanisms as compared with other noble metals, such as Pt and Pd.[8, 15] DFT analysis showed that N_2 adsorption in Ru nanoparticles occurs mainly at the catalytic edge sites of *hcp* Ru (001) with $G = -0.28$ eV, wherein the presence of the adsorbed N_2 species on these edge sites causes the activation of the $N{\equiv}N$ triple bond as it becomes elongated by 0.02 Å as compared with an isolated N_2 molecule in its gaseous phase.[13, 16]

Although Ru-based electrocatalysis in the acidic medium represents an exciting basis for the development of novel electrocatalysts, only a few such catalysts have been studied in acidic medium for their NRR activity.[17-20] For instance, Li et al. synthesized a novel single atom-Ru@rGO/NC electrocatalyst with a high metal loading density which contributed to a NH_3 yield of 110.1 $\mu g\ h^{-1}\ mg_{cat}^{-1}$ and a corresponding FE of 17.9 % at −0.3 V in 0.1 M HCl solution.[19] Moreover, Xu *et al.* have demonstrated that a single-atomic Ru species anchored onto a Ti_3C_2O substrate could give rise to superior activity and selectivity toward electrocatalysts as compared with conventional catalysts with a measured NH_3 yield rate of 27.6 $\mu g\ h^{-1}\ mg^{-1}$ and a corresponding FE of 23.3 % in 0.1 M HCl.[17] Sun *et al.* isolated Ru single atoms within N-doped porous carbon which led to a highly favorable, measured NH_3 formation rate of more than 3.6 $mg_{NH3}\ h^{-1}\ mg_{Ru}^{-1}$; the addition of ZrO_2 to this catalyst effectively suppressed the HER, thereby affording a large FE of up to 21%.[18] Meanwhile, Wang and Sun reported on a Ru_2P-rGO electrocatalyst with an excellent NH_3 yield of 32.8 $\mu g\ h^{-1}\ mg_{cat.}^{-1}$ and a high Faradaic efficiency of 13.0 % at −0.05 V *vs.* RHE in 0.1 M HCl.[20]

There are other recent complementary reports on the electrocatalytic N_2 to NH_3 conversion within different electrolytes. For example, Schechter and coworkers performed a comparative study of RuO_2 and Ru, wherein RuO_2 nanoparticles displayed a 58 % higher ammonia production rate of 16.5 μg h^{-1} cm^{-2} and a FE of 0.26 % at −0.15 V as compared with a Ru black control, characterized by corresponding values of 6.8 μg h^{-1} cm^{-2} and 0.19% FE at −0.15 V vs. RHE in 0.1 M KOH.[8] Finally, a NH_3 yield rate of up to 67.8 ± 4.9 μg h^{-1} mg_{cat}^{-1} coupled with a FE of 19.5 ± 0.6% in 0.1 M K_2SO_4 using Ru–N_4 sites, embedded onto porous carbons, were reported by Zhuang *et al.*[21]

The "gold standard" for either NRR or HER electrocatalysis is nominally a Pt-based material. However, Pt is costly and scarce, thereby making it difficult to incorporate it as part of large-scale industrial applications.[22] By contrast, Ru can be produced at a quarter of the cost of Pt and maintains a rich and complex coordination chemistry.[23] Moreover, Ru displays a higher oxygen affinity than Pt in addition to a greater electronic conductivity, meaning that theoretically, it can better facilitate the desired electrocatalytic conversions.[22] Yet, Ru catalysts tend to cluster, due to their high cohesive energy. To prevent aggregation and to expose the active catalytic sites on Ru, an underlying support often needs to be utilized. One such material is hexagonal boron nitride (h-BN), which has shown great promise in electrocatalytic applications, due to its wide bandgap, thermal stability and conductivity, chemical inertness, and associated dielectric properties.[24] This is typical of many 2D nanomaterials as their electrons can enable mobility along the 2D plane.[24] Hence, h-BN is an ideal structure for supporting RuO_2 nanoparticles; its electrocatalytic properties can be further enhanced by introducing heteroatoms, such as carbon, into its surface. Ma et al. found that C-BN is an effective electrocatalyst for NRR, exhibiting a NH_3 yield of 44.59 ± 1.79 μg/h mg_{cat} at -0.9 V (vs RHE) and a Faradaic efficiency (FE) of 13.27 ± 0.42 % at -0.7 V (vs RHE).[25] Moreover, Salah et al. noted that Ru nanoparticles dispersed onto a BN sheet modified with C gave rise to a small HER overpotential of 32 mV and an associated Tafel slope of 33.89 mV/dec in 1 M KOH. The addition of the nanosheet structure increased the conductivity of BN and the synergistic effects between Ru and BN@C allowed for the improved HER performance in both alkaline and acidic environments.[26] The prior success of carbon doping has motivated this work on exploring the electrocatalytic properties of Ru doped on boron nitride (BN) sheets (Ru-RuO_2@BN).

Moreover, the superiority of BN over the use of traditional carbon supports in terms of chemical inertness, oxidation resistance, thermal stability, and catalyst-support interaction would impart additional benefits of this nitride material as a catalyst support.[27] Hence, we believe that BN represents an especially promising support for effective NRR or HER electrocatalysis. In particular, the unique structure of Ru-RuO_2@BN should allow it to enable high NRR/ HER activity in acidic media under a specified range of potentials. This work therefore details the facile solvothermal synthesis of this novel composite electrocatalyst coupled with an exploration of its NRR and HER activity mainly in acidic media.

2. Experimental

2.1. Materials. Ruthenium (III) acetylacetonate (Beantown Chemical), boron nitride (Beantown Chemical), benzyl alcohol (Thermo Scientific), Nafion solution (5 wt. % in water and ethanol mixture) (Beantown Chemical), Toray carbon paper - 30% wet proofing (Fuel Cell Earth), sodium citrate dehydrate (Fisher Chemical), salicylic acid (Thermo Scientific), sodium hypochlorite solution (NaClO, 5%) (Fisher Chemical), ammonium chloride, potassium nitrate (KNO_3) (Thermo Scientific), sodium hydroxide (NaOH) (Acros Organics), sodium nitroferricyanide dihydrate ($C_5FeN_6Na_2O\cdot 2H_2O$) (LabChem), potassium hydroxide (KOH) (Spectrum Chemical Mfg. Corp.), Glenco polishing cloth (Electron Microscopy Sciences), ethyl alcohol (C_2H_6O, 95.0%) (Thermo Scientific), aluminum oxide polishing compound (Al_2O_3) (Alfa Aesar), and hydrochloric acid (HCl) (36.5-38 %, Alfa Aesar) were all utilized, as received.

All the reagents purchased were of analytical reagent grade. The Ultrapure water (18.2 MΩ cm^{-1}) used in all these experiments was dispensed by a Milli-Q ultrapure system.

2.2. Synthesis of Ru-RuO_2@BN. The Ru-RuO_2@BN electrocatalyst was prepared by mixing in 50 mg BN powder in a solution of 10 mL benzyl alcohol containing ruthenium (III) acetylacetonate (10 % loading, 5 mg); the mixture was then sonicated for 10 min followed by stirring for 30 min. This concoction was transferred to a 23 mL autoclave and later heated at 200°C for 24 h. After 24 h, this solution was subsequently cooled down to room temperature; washed by centrifugation for several times with ethanol and water; and ultimately dried in a vacuum furnace at around 50°C for 24 h to obtain the desired Ru-RuO_2@BN powder.

2.3. Preparation of the Working Electrode for NRR Experiment. The working electrode was prepared using the method associated with our previously accepted protocols.[28] 10 mg of Ru-RuO_2@BN was dispersed in a solution containing 700 μL H_2O, 200 μL isopropyl alcohol, and 100 μL Nafion (5 wt. %). It was then sonicated for 1 h to form a homogeneous ink and a 10 μL aliquot of this ink was later loaded and dried onto a carbon paper on an area of 1 cm × 1 cm such that the measured catalyst loading was 0.1 mg cm^{-2}. The working electrode with the ink was named as C-Ru-RuO_2@BN.

The preparation of the Working Electrode for the HER Experiment has been discussed in the SI.

2.4. Characterization

2.4.1. Scanning electron microscopy (SEM): The SEM images were collected on a JEOL JSM-7600F scanning electron microscope, attached to an energy dispersive spectrometer (EDS) with accelerating voltages in the range of 5 to 10 kV. The Ru-RuO_2@BN sample was prepared by dispersing a small amount in 5 mL of ethanol by sonication and then drop-casting in small aliquots onto silica wafers prior to drying at room temperature.

2.4.2. Transmission electron microscopy (TEM): The Ru-RuO$_2$@BN sample for TEM imaging was generated by dispersing it in 5 mL of ethanol via sonication and drop-casting aliquots onto copper grids covered with a lacey carbon coating. The TEM images were collected using a JEOL 1400 transmission electron microscope at accelerating voltages between 80 and 120 kV; this instrument was equipped with a 2048 × 2048 Gatan charged-coupled device (CCD) camera. The HRTEM and STEM data were also collected using a FEI Talos 200x, which is an operando Scanning Transmission Electron Microscope. The ImageJ software was subsequently used to calculate the particle size.

2.4.3. X-ray Diffraction (XRD): The Ru-RuO$_2$@BN sample for the XRD measurement was prepared by sonicating the Ru-RuO$_2$@BN powder, dispersed in 5 mL of ethanol. Small aliquots of the sample were then drop cast onto a Si zero background diffraction plate. A Rigaku Mini Flex 600 X-ray diffractometer was used to conduct the XRD analysis. Cu Kα radiation (λ = 1.5406 Å) was utilized; the operating voltage-current conditions consisted of 40 kV and 15 mA. The 2θ value measurements were collected from 10°– 80° at a rate of 4°/min, and the Match! Program was subsequently applied to analyze the XRD patterns in conjunction with the underlying JCPDS file numbers 65-1863, 65-2824, and 73-2095.

2.4.4. X-ray photoelectron spectroscopy (XPS): X-ray photoelectron spectroscopy (XPS) measurements were performed on a Physical Electronics Quantum 2000 XPS microprobe instrument (with chemical mapping), equipped with a 16-channel detector, a flood gun for charge compensation (which facilitates surface analysis with limited conductivity), and an ion gun for chemical profiling. A monochromatic Al K α X-ray (1486.6 eV) with a beam diameter of 50 microns was utilized at 12.5 W for the resulting measurements. The associated neutralizer was set at 1.0 V and 20 microamps. We noted that the analyzer was used in the Fixed Analyzer

Transmission (FAT) mode, and the data deconvolution was performed with PHI MultiPak software (version 9.1.1), using a Shirley background for all observed peaks.

2.4.5. X-ray absorption fine structure (XAFS): Ru K-edge XAFS data were collected at the QAS beamline of NSLS-II in fluorescence mode using a PIPS detector. 20 scans were collected and averaged out in order to improve the signal-to-noise ratio. The data were processed and analyzed using Athena software from the Demeter package.

2.4.6. Raman spectroscopy: The Raman spectral analysis for the Ru-RuO_2@BN sample was performed under ambient conditions, using a WiTec alpha 300 apyron in a Quantum material press (QPress) glovebox, equipped with a 532 nm diode laser. The laser was operated at an output power of 5 mW, focused through an x20 (NA = 0.5) objective. The spot size of the laser was ~1.3 μm in diameter. The spectrum was collected using a 1800 grooves/mm grating. Each spectrum was acquired with an integration time of 10 s, and 20 accumulations were averaged to improve signal-to-noise ratio. Data analysis was carried out using the WiTech project software.

2.4.7. Nuclear Magnetic Resonance (NMR): NMR spectra were acquired at room temperature using a 500 MHz spectrometer equipped with a Bruker Avance III console, a Z-gradient unit, and digital variable temperature controls. Data collection consisted of 16 experimental scans and a corresponding 4 control scans.

2.5. Electrochemical NRR Measurements.

The electrochemical NRR experiments were performed on a potentiostat (SP-300, Bio-Logic Science Instruments Ltd.) using Ru-RuO_2@BN, a platinum sheet, and an Ag/AgCl electrode (3M KCl electrolyte) as the working, counter, and the reference electrodes, respectively. To conduct the NRR tests, we used an H-shaped electrolytic cell, which was isolated by a Nafion 211 membrane in the middle, as shown in **Figure S1(a)**. The potential used in the NRR experiment was converted to a reversible hydrogen electrode (RHE) scale by calibration in terms of applying the equation: E (vs. RHE) = E (vs. Ag/AgCl) + 0.209 V. The corresponding current density was normalized to the geometric surface area. For the focal point of our studies, namely electrochemical N_2 reduction, the chronoamperometry tests were initiated from −0.8 to −0.4 V vs. RHE within an N_2 (99.9%)-saturated 0.1 M HCl solution; we purged the chamber with N_2 for about 30 min, prior to running the NRR experiment. The Electrochemical HER Measurements (**Figure S1(b)**), determination and calculation of H_2 have been discussed in the SI.

2.6. Determination of Ammonia (NH_3). A spectrophotometric indophenol blue method was employed to determine the concentration of NH_3 generated after each NRR run.[29] 2 mL of the electrolyte was taken out from the cathodic chamber, and then a mixture of 2 mL of chromogenic reagent (1 M NaOH, 5 wt.% $C_7H_6O_3$, 5 wt.% $C_6H_5Na_3O_7$), 1 mL of oxidizing solution (0.05 M NaClO), and 0.2 mL of catalyzing reagent (1 wt.% $Na_2[Fe(CN)_5NO]$) was added in consecutive steps into this solution. After keeping the mixture in the dark at room temperature for about 1 h, the UV−visible absorption intensity was measured at around 655 nm. The concentration vs. absorbance calibration curves created using a series of different concentrations of the standard NH_4Cl solution were used, as reported in our previous work (**Figure S2**).[28] The fitting curve ($y = 0.077x + 0.0148$, $R^2 = 0.998$) showed a perfect linear correlation between the absorbance values and measured NH_4Cl concentrations.

2.7. Calculation of V_{NH3} and Faradaic Efficiency (FE).

The rate of NH_3 formation (V_{NH3}) was calculated using **Equation 1**.[29-31]

$$V_{NH3} = \frac{V \times [NH_3]}{t \times m_{cat}} \tag{1}$$

The corresponding Faradaic efficiency (F.E.) was calculated using **Equation 2**.[29-31]

$$\mathbf{F.E.} = \frac{\mathbf{3F \times V \times [NH_3]}}{\mathbf{Q \times 17}} \qquad (2)$$

In these equations, V is the volume of the electrolyte; $[NH_3]$ is the concentration of NH_3; t is the electrolysis time; m_{cat} is the catalyst mass; 3 denotes the number of electrons transferred per ammonia molecule; F is the Faraday constant; Q is the theoretical electronic quantity across the electrode; and 17 represents the molar mass of ammonia, which is 17 g/mol.

2.8 Determination of Hydrazine (N_2H_4)

To determine the amount of N_2H_4 formed during NRR within the electrolyte, we used the Watt and Chrisp method.[32, 33] The color reagent needed for this test was prepared by initially dissolving para (dimethylamino)benzaldehyde (PDAB) (5.99 g) in 0.1 M HCl (30 mL) and ethanol (300 mL), as discussed in our previous report.[28] 5 ml of the electrolyte was then mixed with 5 mL of this color reagent and stirred for 30 min at room temperature to form a yellow-colored azine complex. The absorbance readings were measured at 455 nm using a UV−visible spectrometer. A standard curve plotted previously using a series of standard hydrazine solution concentrations of 0.05, 0.1, 0.15, 0.2, 0.3, 0.4, and 0.5 $\mu g\ mL^{-1}$, respectively, in 0.1 M HCl was used as a standard to calculate the amount of hydrazine within the electrolyte (**Figure S3**).

3. Results and Discussion

The Ru-RuO_2@BN electrocatalyst was obtained by a simple solvothermal procedure, wherein a mixture of BN powder and ruthenium (III) acetylacetonate in benzyl alcohol was heated in an autoclave for 24 h at 200 °C. The mixture was subsequently washed by centrifugation several times with ethanol and water to remove any unreacted material and then dried to obtain the desired homogeneous powder of Ru-RuO_2@BN. Both metallic and oxidized Ru have been identified as effective candidates for NRR and HER. DFT calculations have shown that Ru maintains an appropriate nitrogen adsorption energy and overpotential that is lower than that of other noble metals, which collectively render it suitable for NRR.[34] With respect to HER, oxidized Ru species can drive the water splitting reaction whereas metallic Ru atoms can encourage molecular hydrogen production, in accordance with DFT studies.[35] By supporting Ru onto a porous, stable material such as BN, Ru and RuO_2 particles tend to be uniformly distributed and the amount of exposed active sites for electrocatalysis is maximized. Additionally, the Ru-RuO_2@BN composite material allows for synergistic effects between the Ru and BN, thereby further improving its catalytic properties.[26] Evidence of cubic boron nitride (c-BN) formation suggests a potential enhancement in the material's observed electrocatalytic activity, in terms of modulating electronic properties, introducing active sites, and enhancing conductivity.[36] A schematic representation for the synthesis of Ru-RuO_2@BN is shown in **Figure 1**.

3.1. Microscopy and Spectroscopy Characterization of Ru-RuO_2@BN

The morphological details of the Ru-RuO_2@BN catalyst were analyzed using SEM equipped with EDS and TEM. The SEM image revealed that Ru and RuO_2 species are dispersed over the layers of BN, as shown in **Figure S4**. However, some aggregated clusters of Ru and RuO_2 were also observed on the BN. The EDS mapping image highlights the presence of Ru, O, B, and N, wherein Ru and O are dispersed over the surface of BN (**Figure S4 (b), (c), (d), (e**)). Although the Ru loading used during the synthesis was expected to be 10%, the actual loading was found to be 5 wt.% as seen in **Figure S4 (f) and (g)**. The ratio of Ru to O suggested that some elemental Ru is also located within the material along with RuO_2. The presence of all the elements was further confirmed by line mapping (**Figure S5**), which reveals that Ru, O, B, and N atoms appear to be dispersed all over, along with some aggregated Ru particles. No carbon traces from the used benzyl alcohol were observed in the EDS as the sample was washed several times with ethanol and water.

To obtain more insight on the actual structural morphology of Ru-RuO_2@BN, we performed TEM analysis (**Figure 2**). The isolated particles of Ru-RuO_2 appeared to be well dispersed on the BN layer with an average size of 2.47 nm, as shown in the histogram in **Figure S6**. To further confirm the crystallinity, we collected HRTEM data (**Figure 2**), which highlighted lattice spacings of ~0.32 nm, corresponding to the (110) plane of the RuO_2.[37, 38] In addition, some amorphous regions were also observed, which could be ascribed to the presence of elemental Ru, thereby suggesting a mixture of two components, i.e. RuO_2 and Ru, within the particle. Due to the smaller overall particle size of 2.47 nm, it was difficult to further resolve the substructure of the particle. For the BN layer itself, an expected lattice spacing of 0.22 nm corresponding to the (100) plane was also observed.[39]

The XRD peak values of Ru-RuO_2@BN of 27.4° and 55.6° were observed, as shown in **Figure S7(a)**. It is worth noting that these two peaks likely originated from the BN (002) and (110) planes, respectively.[40] To confirm this assertion, we calculated the particle sizes using the Scherrer formula and found them to be 21.5 nm, i.e. similar to the value of 29.3 nm found from the XRD pattern of the precursor h-BN (**Figure S7(b))**. The lack of XRD peaks originating from either Ru or RuO_2 can be ascribed to the small amount of Ru/RuO_2 (Ru wt.% = 5), which would have contributed to either a very weak or no signal at all, as compared with the underlying BN matrix, thereby rendering the diffraction peaks from Ru/RuO_2 as effectively undetectable. The lack of discernible Ru/RuO_2 XRD peaks in Ru-RuO_2@BN limits phase identification, attributed to the material's amorphous character and the small size of the nanoparticles (~2.47 nm).

However, to further confirm the presence of Ru/RuO_2, we have conducted a series of XPS and XAS analyses. Specifically, the X-ray photoelectron spectroscopy (XPS) studies of Ru-RuO_2@BN (**Figure S8(a)**) suggested the occurrence of B *1s*, N *1s*, O *1s*, Ru *3d* and Ru *3p* peaks which are consistent with the presence of a Ru-RuO_2 structure on the BN layers. The B *1s* spectra from the Ru-RuO_2@BN demonstrate the presence of a peak at 190.2 eV associated with the B-N bond (**Figure S8 (b)**).[41-43] The N *1s* spectra highlighted in **Figure S8 (c)** indicate an N-B bond associated with a peak appearing at 397.8 eV.[42, 44] The O *1s* region (**Figure S8 (d)**) shows two major peaks present at 530.4 eV and 532.2 eV, that can be assigned to RuO_2 and C=O, respectively,[41, 45-47] along with a peak at 533.7 eV, that can be identified with a O-C=O bond.[41] The C and O elements observed here may have originated either from oxygen contamination or from CO_2 absorbed onto the surface of Ru-RuO_2@BN.[41] The Ru *3p* regions are represented in **Figure S8 (e)**, featuring the presence of $3p_{3/2}$ singlets of Ru and RuO_2 with peaks positioned at 461.1 eV and 463.3 eV, respectively.[46, 47] Furthermore, the Ru *3d* regions as shown in **Figure S8 (f)**, underlie the occurrence of doublets associated with signals that can be ascribed to Ru (280.0 eV (Ru $3d_{5/2}$) /284.2 eV (Ru $3d_{3/2}$)) and RuO_2 (281.3 eV (Ru $3d_{5/2}$) /285.5 eV (Ru $3d_{3/2}$)).[46, 47]

The normalized XAS data in energy space for Ru-RuO_2@BN and Ru (metal) and RuO_2 reference spectra are shown in **Figure 3 (a)**. The extended XAFS (XAFS) data in k-space, and r-space for Ru-RuO_2@BN and Ru (metal) and RuO_2 reference spectra are shown in **Figure 3 (b)**, and **(c)**. The presence of multiple isosbestic points is clearly observable in the energy and k-space plots (**Figure 3 (a)** and **(b)**). These results indicate that the Ru-RuO_2@BN data likely consists of a mixture of the two states of Ru, i.e., oxidized and metallic. However, these results do not indicate that the sample is indeed a combination of bulk RuO_2 and Ru metal states, because the x-ray absorption near-edge structure (XANES) region does not contain relevant data about the long-range order of Ru phases, but rather merely their oxidation states and local structures. Therefore, the information about the Ru-O and Ru-Ru coordination numbers was obtained by a quantitative fitting analysis of Ru extended X-Ray absorption fine structure (EXAFS) spectra.

The Ru foil EXAFS data were processed first to determine the amplitude factor. The K-range incorporates 2-13 $Å^{-1}$; the r-range for the fit spans 1-2.816 Å. The results are provided in **Figure S9** and in **Table S1**. The S_0^2 factor was fixed to 0.75, and the theoretical contributions were noted for Ru-Ru (from bulk Ru model) and Ru-O (from RuO_2 model). The k-range varies from 2 to 13 $Å^{-1}$ with an r-range for the fit of 1-3 Å. The results are presented in **Figure 3 (d)** and in **Table S1**. Based on the XANES/EXAFS results, we assert that there are regions of oxidized and reduced Ru. However, the XANES/EXAFS data do not allow us to effectively conclude whether they are within the same particle (e.g., a proposed configuration consisting of a Ru metal core and an RuO_x shell).

The Raman spectral data were collected at specific locations of Ru-RuO_2@BN and are shown in **Figure S10**. As per theoretical prediction, the single crystal rutile RuO_2 maintains characteristic Raman bands located at 528, 646 and 716 cm^{-1} for the E_g, A_{1g}, and B_{2g} vibration modes, respectively.[48] The Raman spectra of Ru-RuO_2@BN demonstrated peaks located at 495 (E_g), 617 (A_{1g}), and 710 (B_{2g}) which are characteristic of the red shift of the peak positions as compared with those of the single crystal rutile RuO_2; these findings can possibly be ascribed to its nanoscopic nature.[48] The peak positioned at 1369 cm^{-1} corresponds to the E_{2g} mode within the h-BN layer, whereas the longitudinal optical (LO) and transverse optical (TO) modes of some h-BN which had converted to c-BN highlighted prominent Raman peaks located at 1307 cm^{-1} (LO) and 1077 cm^{-1} (TO), respectively (**Figure S10**).[49]

3.2. Electrocatalytic Performance of Ru-RuO$_2$@BN

A mass loading of 0.1 mg cm^{-2} of the as-synthesized Ru-RuO$_2$@BN catalyst was painted onto carbon paper (CP) forming the cathode electrode (C- Ru-RuO$_2$@BN) for NRR within the H-shaped electrolytic cell. A linear sweep voltammetry curve for C- Ru-RuO$_2$@BN within the Ar- and N$_2$-saturated 0.1 M HCl solution was recorded, as illustrated in **Figure S11**. The LSV measurement was performed in Ar-saturated 0.1 M HCl to establish a baseline for non-faradaic and background processes on the Ru-RuO$_2$@BN surface. The negligible variation in current density observed under Ar suggested that the HER and other parasitic reactions are significantly suppressed on the catalyst surface under the experimental conditions. Chloride ions are relatively unreactive and maintain a weaker adsorption on many catalyst surfaces as compared with sulfate and perchlorate ions from acids like $H_2SO_4^{2-}$ and $HClO_4^{-}$. Hence, 0.1 M HCl was used as the electrolyte, because the Cl- ions are less likely to block active sites, thereby allowing for more efficient nitrogen adsorption and subsequent reduction reactions.[50, 51]

It was observed that the current density measured in the N$_2$-saturated 0.1 M HCl solution was much higher than that within the Ar-saturated 0.1 M HCl solution. The LSV curves suggested that the electroreduction of N$_2$ to NH$_3$ occurred with an onset potential of around −0.5 V on the C- Ru-RuO$_2$@BN electrode.

The electroreduction data of N$_2$ to NH$_3$ using Ru-RuO$_2$@BN as electrocatalysts are shown in **Figures 4 (a)**, **4 (b)**, **5 (a)**, and **5 (b)**. Stable chronoamperometry curves (i.e., time-dependent current density curves) of C- Ru-RuO$_2$@BN were observed at various potentials (**Figure 4(a))**. The current density started off at a high current for all the different potentials from -0.4 V to -0.8 V, dropped and leveled off, and consequently achieved a threshold value. This observation can be ascribed to the charging of the double layer coupled with a local reduction in concentration of H^+ and N_2 near the electrode surface, as seen in our previous work.[28, 29, 51]

The electroreduction process associated with the production of NH_3 was run for 2 h, and after that, the as-generated NH_3 dissolved within the electrolyte (0.1 M HCl) was detected using the indophenol blue method,[52-54] wherein the absorbance peak at 655 nm for indophenol could be analyzed to quantify the amount of NH_3 formation. The UV-visible spectra obtained at different potentials after the chromogenic reactions of the NH_3 dissolved electrolyte are shown in **Figure 4(a)**. Based on our previously obtained calibration curves ($y = 0.077x + 0.0148$, $R^2 = 0.998$, **Figure S2**),[28] we calculated the amount of as-generated NH_3 per hour and per microgram of the catalyst, along with accompanying V_{NH3} and FE values (**Figure 5(a)** and **Table 1**). At -0.4 V, a smaller V_{NH3} of 9.75 μg h^{-1} mg^{-1} and FE of 40.8% were observed, which is not surprising given that the potential applied was insufficient to initiate NRR. It is evident that the highest V_{NH3} of 16.8 μg h^{-1} mg^{-1} and FE of 52.9 % were noted at a potential of -0.5 V. However, at -0.6 V, the V_{NH3} and FE again decreased to lower V_{NH3} and FE values of 12.3 μg h^{-1} mg^{-1} and 29.3%, respectively, which can be attributed to the competing presence of the hydrogen evolution reaction (HER). Furthermore, there was a slight increase noted in V_{NH3} at -0.7 V and at -0.8 V, though the FE decreased gradually at these higher potentials. This apparent increase in V_{NH3} could be ascribed to the greater driving force provided by the higher potential, thereby allowing for a more efficient adsorption and reduction of N_2 on the electrocatalyst surface. However, exceeding the potential resulted in HER, leading to a decrease in the overall FE. The lower FE values measured at -0.7 and -0.8 V could also be ascribed to the increased theoretical electronic quantity expected ($FE \propto 1/Q$) across the electrode.[28]

To enable a comparison of the activities of our catalyst with previously studied NRR electrocatalysts, we have listed these in **Table S2**. It is evident that the performance of our Ru-RuO_2@BN catalyst in selectively yielding NH_3 alone is either superior to or comparable with the activities of the previously reported Ru-based catalyst systems. For instance, Cheng *et al.* reported on a Ru/TiO_2 catalyst, which evinced a low NH_3 yield of 2.11 μg h^{-1} mg^{-1} and an FE of 0.25% at a potential of -0.15 using 0.1M KOH.[55] Similarly, a rGO-based Ru catalyst gave rise to a low NH_3 yield of 9.14 μg h^{-1} mg^{-1} using 0.1 M H_2SO_4 at -0.2 V in the presence of a costlier rGO support.[56] Other reports on bimetallic catalysts, such as PdRu nanorods and PdRu tripods, demonstrated comparatively better NH_3 yields of 34.2 and 37.2 μg h^{-1} mg^{-1}, respectively. However, the same catalyst indicated a very small FE of 2.4 and 1.85 %, respectively. Moreover, it is worth noting that these catalysts incorporated an additional active but nevertheless more expensive Pd elemental content.[57, 58]

We also performed a control experiment to check the formation of NH_3 is only resulting from NRR using C- Ru-RuO_2@BN species and not from any other competing processes. In the experiment, we performed the NRR with only immersing the sample in an N_2-saturated solution deprived of any applied voltage for 2 h. No noticeable production of NH_3 was detected.

We conducted the NRR experiment C- Ru-RuO_2@BN in 0.1 M KOH to assess the effect of the alkaline medium on the production of NH_3. In order to observe the difference in NRR in the acidic and alkaline medium, we kept all the other parameters intact for the experiment. The Ru-RuO_2@BN catalyst did not evince any sufficient NRR activity at a potential of -0.5 V for 2 h, as shown in **Figure S12**. This finding could pertain to the competition between the OH- ions with the N_2 molecules for active sites on the catalyst, which may perhaps lead to reduced N_2

molecular adsorption on the external catalyst surface.[28] As such, this explanation could possibly account for the lower NRR activity of the catalyst for NH_3 formation in an alkaline medium.

Using a method similar to the nitrogen reduction reaction (NRR), the electrocatalytic activity of the Ru-RuO_2@BN catalyst for nitrate reduction (NORR) was evaluated (**Figure S13**). After a 2-hour electrolysis at -0.5 V in a 0.1 M KNO_3 and 0.1 M HCl solution, the resulting NH_3 was detected using the indophenol blue method. Chronoamperometric analysis indicated a reasonable level of stability. The indophenol test yielded a UV-visible absorption peak at 655 nm, confirming NH_3 production. The NH_3 concentration was 0.05 μg/mL, corresponding to a formation rate of 7.15 $\mu g_{NH3}\ h^{-1}\ mg^{-1}$, which is less than the NH_3 formed in the NRR experiment of Ru-RuO_2@BN under similar reaction conditions. This finding revealed that Ru-RuO_2@BN is also effective in NORR and could possibly lead to another study on its efficiency in NORR. However, in keeping our scope limited to the NRR studies, we did not perform further investigations to confirm the NH_3 production from NORR.

The stability and durability of electrocatalysts are critical for their practical applicability. To assess these metrics for the Ru-RuO_2@BN catalyst, a chronoamperometry test was conducted at -0.5 V for 24 hours, as shown in **Figure 5 (b)**. The catalyst evinced good stability, maintaining a consistent current density under NRR electrolysis conditions, associated with a strong acid medium and constant charge-discharge cycles. Furthermore, the catalyst's reusability was confirmed through four consecutive recycling tests, as illustrated in **Figure 6 (a)** and **Figure 6 (b)**. Using the same C-Ru-RuO_2@BN electrode, the measured V_{NH3} and FE remained largely unchanged across all cycles (**Figure 6 (a)**). These findings collectively demonstrate the catalyst's excellent durability and recyclability of Ru-RuO_2@BN.

The structural stability of the C-Ru-RuO_2@BN electrode was investigated using Raman spectroscopy following the recyclability and stability tests. As shown in **Figure S14,** the Raman spectra of the post-test samples, both after a 24-hour stability test (**Figure S14 (a)**) and after the 4th NRR cycle (**Figure S14 (b)**), show essentially identical Raman shifts to that of the Ru-RuO_2@BN catalyst itself (**Figure S10**). The analysis demonstrated that the characteristic peaks corresponding to the RuO_2, and c- and h-BN species were unchanged, both before and after the NRR process, thereby confirming the material's stability under the tested conditions.

To verify that the morphology, composition, and performance of the catalyst Ru-RuO_2@BN can persist in its comparative stability after the catalyst stability test, we have conducted an SEM-EDS analysis of the used catalyst, as shown in **Figure S15**. The results confirmed that the morphology, chemical composition, and integrity of the catalyst remained stable, with Ru, O, and N maintaining a relatively uniform distribution throughout the material. The EDS mapping of minor impurities from carbon (specifically from carbon paper) is not shown for the sake of clarity of a meaningful comparison with the original Ru-RuO_2@BN catalyst. The stability testing confirms that the Ru-RuO_2@BN catalyst is highly robust. The material's morphology, chemical composition, and overall integrity were fully preserved, thereby indicating its promise for long-term applications.

During a functional NRR process, hydrazine (N_2H_4) can be released as a byproduct along with ammonia, and it can act as an active intermediate.[59-62] The formation of N_2H_4 is mechanistically relevant only as an intermediate species ($^*N_2H_4$) and not as a product (N_2H_4). As an intermediate, it is highly unstable and could finally lead to the formation of a more stable product, namely ammonia (NH_3). We used the Chrisp and Watt method to detect the presence or absence of N_2H_4,[32] using the standard curve for the N_2H_4 assay from our previous report (**Figure**

S3).[28] It was found that the concentration of N_2H_4 in the resulting electrolyte after NRR was negligible at all electrolysis potentials analyzed from -0.4 V to -0.8 V (**Figure S16**). These data are in strong agreement with the excellent selectivity toward NH_3 production associated with the Ru-RuO_2@BN electrocatalyst.

As HER is known to interfere with NRR as both reactions occur on the same electrode, we attempted to check the HER activity of the same catalyst using the same acidic media. Although, for HER we had to use a different electrocatalytic setup to ensure proper experiment using a rotating disk electrode (RDE). For the HER experiment, the glassy carbon working electrode was prepared, and the HER was conducted, according to the procedures described in SI. A linear sweep voltammetry curve for Ru-RuO_2@BN within an Ar-saturated 0.1 M HCl solution was recorded, as illustrated in **Figure S17(a)**. Surprisingly, a significant rise in current density was detected at a potential of ~-0.2 V (vs RHE), indicating the possible onset of H_2 production. This shift in the onset potential in the LSV of HER as compared with the LSV seen in NRR experiment (**Figure S11**) might be ascribed to the use of a completely different electrochemical setup and catalyst loading associated with the HER experiment, as compared with the catalyst loading used in the analogous NRR experiment (i.e., 0.25 mg cm^{-2} for HER and 0.1 mg cm^{-2} for NRR). Also, while conducting the HER experiment, an IR correction (10 Ω) was performed. Within the H cell, the H_2 production itself was confirmed with the aid of the combustible gas leak detector.

To quantify the extent of the electrocatalytic performance of Ru-RuO_2@BN, overpotential and Tafel slope were calculated using the values from LSV within a potential window of -0.6 V to 0.4 V. **Figure S17** highlights a typical LSV of Ru-RuO_2@BN in 0.1 M HCl, using the setup shown in **Figure S1(b)**. A sharp rise in current density is observed, starting at around -0.2 V, indicating the possible onset of HER. Multiple experimental runs demonstrated that in 0.1 M HCl, Ru-RuO_2@BN yielded an overpotential of 437 mV at a current density of 10 mA cm^{-2}. Tafel analysis indicated that in 0.1 M HCl, Ru-RuO_2@BN possessed a Tafel slope of 246.3 mV dec^{-1} (**Figure S17 (b)**). These data suggests that Ru-RuO_2@BN displayed a poor HER activity in an acidic medium. The low HER activity observed might be ascribed to the competition between HER and NRR around -0.4 V, which also explains the considerably low NRR activity at -0.4 V (V_{NH3} = 9.75 ± 0.85 μg h^{-1} mg^{-1}). By contrast, the production of NH_4 is likely to be more thermodynamically and kinetically favorable than the production of H_2 on this catalyst at -0.5 V (V_{NH3} = 16.8 ± 1.0 μg h^{-1} mg^{-1}). The presence of NRR species has been known to suppress HER activity, which may also explain the relatively low HER activity observed.[1]

A cyclic voltammetry curve for Ru-RuO_2@BN within an Ar-saturated 0.1 M HCl solution was recorded, as illustrated in **Figure S18**. It can be observed that between 0.25 V - 1.25 V, no Faradaic processes occur. To quantify surface area, cyclic voltammetry was performed on the sample within this potential window at a scan speed of 2 – 14 mV s^{-1} (**Figure S19 (a)**). Since surface area is directly proportional to the double layer capacitance (C_{DL}) according to **Equation S2** (in the SI), C_{DL} was calculated to quantify the surface area of Ru-RuO_2@BN. The average 2 C_{DL} value of Ru-RuO_2@BN was noted to be 0.00264 F cm^{-2} (**Figure S19 (b)**). This C_{DL} is lower than other reported literature values (**Table S3**), thereby suggesting that Ru-RuO_2@BN maintains a small surface area and contains relatively few catalytically active sites. Since the CV gave rise to a small current at a potential of 2 V, we did not attempt to further verify the oxygen evolution reaction (OER) activity of this catalyst as it was likely not to be overly high.

We have also listed a comparison of activities of our catalyst with previously studied HER electrocatalysts (**Table S3**), to further our understanding of our catalyst's selective NRR activity. It is clear that our Ru-RuO_2@BN catalyst evinces poor HER performance as compared with some previously reported Ru-based catalyst systems. For example, a study conducted by Dang *et. al.* observed a low overpotential of 16 mV in a 0.5 M H_2SO_4 electrolyte for Ru/RuO_2.[63] Similarly, Yang *et. al.* found that W- and La-doped RuO_2 materials gave rise to high HER activity in alkaline media (1 M KOH electrolyte). W-RuO_2 yielded the lowest overpotential (29 mV) and Tafel slope (24 mV dec^{-1}) of the three electrocatalysts tested.[64] The suppression of HER in Ru-RuO_2@BN can likely be attributed to the catalyst's preference for NRR which further confirms the material architecture's ability to be an effective NRR electrocatalyst. However, it is to be noted that most of these other reported systems used H_2SO_4 as the electrolyte and not HCl. The HER activity of our catalyst may show enhanced activity in either similar H_2SO_4 or other alkaline media, a point which has not been taken into consideration in this current study but could have a potential future scope to explore.

To verify the origin of NH_3 formation during Ru-RuO_2@BN-catalyzed NRR, we recorded ^1H NMR spectra of the NH_4^+ species in the electrolyte. As shown in **Figure 7 (a)**, the ^1H NMR spectrum for standard NH_4Cl exhibits a characteristic 1:1:1 triplet at 7.09, 6.99, and 6.91 ppm (blue curve), resulting from the spin-spin coupling between the proton and the ^{14}N nucleus ($I = 1$). Concentrations of NH_4Cl exhibited a strong linear correlation with the magnitude of the ^1H NMR signals at 6.99 ppm. For the tested sample of Ru-RuO_2@BN (electrolysis at −0.5 V), the spectrum revealed a distinctive 1: 1: 1 triplet centered at 7.00 ppm, with peaks at 7.10, 7.00, and 6.91 ppm (maroon curve). The standard curve (**Figure 7 (b)**) suggested an NH_4^+ concentration of 0.11 μg mL^{-1} for the test sample. This value correlates well with the 0.13 μg mL^{-1} measurement obtained using the indophenol blue method, as detailed in **Table 1**.

To further verify the nitrogen source of the synthesized NH_3, we performed a $^{15}N_2$ isotopic labeling experiment, along with additional control experiments to exclude contamination from air, water, electrolytes, or the catalyst, in order to confirm that the detected NH_3 was not derived from external impurities. As shown in **Figure 7 (a)**, the ^1H NMR spectrum of the $^{15}NH_4Cl$ standard sample (green curve) exhibited a characteristic doublet coupling at 7.05 and 6.92 ppm, distinguishing it from the triplet observed for the standard $^{14}NH_4Cl$. During the NRR conducted over Ru-RuO_2@BN catalyst in $^{15}N_2$-saturated electrolyte (−0.5 V), the ^1H NMR spectrum (red curve) displayed a doublet at 7.05 and 6.91 ppm. The signal matched that noted for the $^{15}NH_4Cl$ standard, confirming that the as-produced NH_3 originated from the supplied N_2 gas.

Furthermore, we have performed blank indophenol experiments in the absence of N_2 (i.e., only pure Ar gas was passed through the system) and in the absence of the catalyst using ultrapure water and electrolytes while ensuring that the environment associated with the equipment is sufficiently inert so as to avoid inadvertently introducing nitrogen-containing contaminants and impurities. In the absence of N_2 (i.e., only pure Ar gas was put through the system) and the catalyst, no absorbance peak at around 655 nm was observed in the UV-visible spectra in both cases, when the experiment was carried out in 0.1 M HCl after 2 h of electrolysis, as measured against a potential of -0.5 V (**Figure S20**). This set of results reinforces our conclusions herein.

According to the DFT calculations, for NRR with metal-based catalysts, the possible pathways which are expected to be involved with the process are the associative and dissociative pathways of N_2, along with the dissociative pathways of NNH_2, $HNNH_2$, and H_2NNH_2.[13] Dabin and coworkers utilized Ru nanoparticles (Ru NPs) as an electrocatalyst for electrochemical NRR in a 0.01 M HCl aqueous solution. The DFT analysis revealed that the catalytic edge sites of hcp

Ru (001) NP were primarily responsible for the adsorption of N_2. The adsorbed N_2 molecule on edge sites caused the N=N triple bond to be activated, as it is 0.02 Å more elongated than an isolated N_2 molecule in the gas phase.[13, 65] HyungKuk et al. studied the role of CeO_2/RuO_2 nanolayers on vertical graphene catalyst in NH_3 generation. In their DFT studies, they found that for the RuO_2 (110) surface, the highest free energy change resided in the first hydrogenation step from *NN to the *NNH intermediate with an overpotential of 0.76 V. The activation energy for the two steps in the RuO_2 NRR path was calculated, wherein the activation barrier for the step of $*NN + *H \rightarrow *NNH$ was found to be 0.86 eV and for the step of $*NH_2 + *H \rightarrow *NH_3$, the calculated energy barrier was computed to be 0.45 eV. These energy barriers were comparatively low and can be easily overcome under ambient conditions. Hence they suggested that the use of RuO_2 can reduce the input of external electric energy into the system for the NRR.[66]

The effective activation of N_2 molecules with an extremely low reaction barrier occurs via an associative mechanism, which is facilitated by the interaction between Ru's *d*-orbitals and the σ and π bonding and the anti-bonding orbitals of N_2.[67] Kim et al. studied the adsorption geometry of N_2 on RuO_2 (110) using quantitative LEED and DFT calculations. They found that the N_2 molecules sit above the coordinatively unsaturated Ru atoms, which can dominate the observed activity of the RuO_2 (110) surface.[68, 69] In our catalyst, Ru-RuO_2@BN, N_2 is expected to interact with the Ru centers of either Ru or RuO_2. However, current evidence is insufficient to confirm whether these species coexist either within a single discrete nanoparticle or as separate distinctive domains.

The associative mechanism is the most common model proposed in DFT studies for the low-temperature, low-pressure NRR on metal surfaces. This mechanism begins with the end-on adsorption of the nitrogen molecule ($*N_2$) onto the catalytic surface. The N_2 triple bond is then broken via a series of reduction steps, which proceed through either the alternating pathway or the distal pathway. In the alternating pathway, the N_2 molecule initially adsorbs onto the surface, followed by three hydrogenation steps that produce the first ammonia molecule. Subsequently, the $^*NH_2$ intermediate combines with H^+ to form a second NH_3 molecule. By contrast, the distal pathway involves hydrogenation, occurring exclusively on one nitrogen atom until the first NH_3 is formed, essentially leaving a *N species adsorbed on the surface. This remaining *N species then undergoes two further hydrogenations, which initially generate $^*NH_2$, before ultimately producing the second NH_3 molecule.[70] While both alternating pathway and the distal pathways are possible, we have proposed an associative alternating pathway (**Figure 8**), in which the $^*N_2$ molecule first adsorbs onto the surface of Ru, followed by the hydrogenation steps that end up generating *NNH, *NHNH, $^*NHNH_2$, and $^*NH_2NH_2$ species, all of which can lead to NH_3 formation. Moreover, the $^*NH_2$ intermediate can combine with H^+ to form NH_3 as well.

4. **Conclusions**

We have studied the electrochemical activity of a Ru-RuO_2-decorated boron nitride (BN) catalyst towards NRR. The NRR experiments highlighted a V_{NH3} of 16.8 µg h^{-1} mg^{-1} and a corresponding Faradaic efficiency (FE) of 52.9 % at a potential of -0.5 V. This FE value is higher than that of most of the recently reported Ru-based catalysts. Moreover, the similar intrinsic activity of Ru, as compared with alternative catalysts incorporating more costly metals, implies that our reported system herein is not only cheaper in cost but also favorably competitive in terms of both its activity and durability. These advantages render our catalyst as an ideal option and substitute to most of the recently reported catalysts.

In general, Ru- based catalysts have rarely been explored for HER using HCl as the electrolytic media. Since we used HCl as the electrolyte for NRR, we have attempted to check its HER activity under similar conditions to understand its interference with NRR. Herein, we have shown that, for HER, Ru-RuO_2@BN yielded an η of 0.43 V at a current density of 10 mA cm^{-2} and a Tafel slope of 246.3 mV dec^{-1} in 0.1 M HCl. This low activity makes it clear that the catalyst Ru-RuO_2@BN is not suitable for HER in acidic conditions.

In summary, this study demonstrates the effective NRR performance of an inexpensive Ru-RuO_2@BN catalyst and suggests a clear path for future studies, including a more comprehensive evaluation of the competing hydrogen evolution reaction (HER) and the development of new catalysts and electrolyte systems.

Supporting Information: Electrocatalytic experiment setup photograph; NH_4Cl and hydrazine calibration curves; structural and chemical characterization data of the samples, including SEM, size distribution, XRD, XPS and Raman analysis; electrochemical information such as (i) all LSV curves, (ii) chronoamperometric results in KOH and NORR, (iii) indophenol UV−visible curves in KOH and NORR, (iv) Raman and SEM analysis before and after NRR, (v) hydrazine test plots, (vi) LSV for HER, (vii) CV, (viii) chronoamperometric and indophenol UV−visible curves for control experiments, (ix) XAFS table, (x) NRR and HER activity comparison table, and (xi) HER experimental setup in addition to H_2 determination and calculation details.

Author Contribution: Mitu Sharma: Methodology, conceptualization, validation, investigation, data collection, visualization, writing-original draft – review & editing. **Leela Sotsky:** data collection, writing and editing. **Suji Park:** Raman data collection. **Kotaro Sasaki:**

conceptualization, methodology. **Anatoly I. Frenkel:** XAS data collection, analysis and modeling, and XAS discussion. **Gary Halada:** XPS data collection and XPS discussion. **Stanislaus S. Wong:** supervision, resources, project administration, funding acquisition, conceptualization, validation, writing – original draft.

Acknowledgments: We thank Francis Picart from the Department of Chemistry at Stony Brook University for his assistance with setting up the NMR experiments. We acknowledge Michael Gallagher for helpful discussions. The experiments in this work were financially supported by seed grant funding through the Office of the Vice President for Research at Stony Brook University. The authors thank Fernando Camino and Kim Kisslinger for their assistance with HRTEM data collection at the Center for Functional Nanomaterials located in BNL which is supported by the U.S. Department of Energy under Contract No. DESC0012704. A.I.F. acknowledges support of XAFS data analysis by the U. S. National Science Foundation award 2452446. The catalytic activity measurements were supported in part by the Division of Chemical Science, Geosciences, and Bioscience of the Office of Basic Energy Sciences at the U.S. Department of Energy (DOE) under Contract No DESC0012704. This research used the Quantum material press (QPress) of the Center for Functional Nanomaterials (CFN), which is a U.S. Department of Energy Office of Science User Facility, at Brookhaven National Laboratory under Contract No. DE-SC0012704. This research used beamlines 7-BM (Quick X-ray Absorption and Scattering, QAS) the National Synchrotron Light Source II, a Department of Energy (DOE) Office of Science User Facility operated by Brookhaven National Laboratory under Contract DE-SC0012704. Beamline operations were supported in part by the Synchrotron Catalysis Consortium (DOE Office of Basic Energy Sciences Grant DE-SC0012335).

References

(1) Wu, T.; Melander, M. M.; Honkala, K. Coadsorption of NRR and HER intermediates determines the performance of Ru-N_4 toward electrocatalytic N_2 reduction. ACS Catal. 2022, 12 (4), 2505-2512. DOI: 10.1021/acscatal.1c05820.

(2) Chen, J. G.; Crooks, R. M.; Seefeldt, L. C.; Bren, K. L.; Bullock, R. M.; Darensbourg, M. Y.; Holland, P. L.; Hoffman, B.; Janik, M. J.; Jones, A. K. Beyond fossil fuel–driven nitrogen transformations. Science 2018, 360 (6391), 873. DOI: 10.1126/science.aar6611.

(3) Qing, G.; Ghazfar, R.; Jackowski, S. T.; Habibzadeh, F.; Ashtiani, M. M.; Chen, C.-P.; Smith III, M. R.; Hamann, T. W. Recent advances and challenges of electrocatalytic N_2 reduction to ammonia. Chem. Rev. 2020, 120 (12), 5437-5516. DOI: 10.1021/acs.chemrev.9b00659.

(4) Chen, J.; Cheng, H.; Ding, L.-X.; Wang, H. Competing hydrogen evolution reaction: a challenge in electrocatalytic nitrogen fixation. Mater. Chem. Front. 2021, 5 (16), 5954-5969. DOI: 10.1039/D1QM00546D.

(5) Yang, W.; Chen, S. Recent progress in electrode fabrication for electrocatalytic hydrogen evolution reaction: A mini review. Chem. Eng. J. 2020, 393, 124726. DOI: 10.1016/j.cej.2020.124726.

(6) Ismael, M.; Wark, M. A recent review on photochemical and electrochemical nitrogen reduction to ammonia: Strategies to improve NRR selectivity and faradaic efficiency. Appl. Mater. Today 2024, 39, 102253. DOI: 10.1016/j.apmt.2024.102253.

(7) Qiao, Z.; Johnson, D.; Djire, A. Challenges and opportunities for nitrogen reduction to ammonia on transitional metal nitrides via Mars-van Krevelen mechanism. Cell Rep. Phys. Sci. 2021, 2 (5), 100438. DOI: 10.1016/j.xcrp.2021.100438.

(8) Velayudham, P.; Schechter, A. A comparative study of RuO_2 and Ru reveals the role of oxygen vacancies in electrocatalytic nitrogen reduction to ammonia under ambient conditions. Appl. Catal., A 2023, 665, 119375. DOI: 10.1016/j.apcata.2023.119375.

(9) Deng, T.; Cen, C.; Shen, H.; Wang, S.; Guo, J.; Cai, S.; Deng, M. Atom-pair catalysts supported by N-doped graphene for the nitrogen reduction reaction: d-band center-based descriptor. J. Phys. Chem. Lett. 2020, 11 (15), 6320-6329. DOI: 10.1021/acs.jpclett.0c01450.

(10) Zheng, M.; Xu, H.; Li, Y.; Ding, K.; Zhang, Y.; Sun, C.; Chen, W.; Lin, W. Electrocatalytic nitrogen reduction by transition metal single-atom catalysts on polymeric carbon nitride. J. Phys. Chem. C 2021, 125 (25), 13880-13888. DOI: 10.1021/acs.jpcc.1c03425.

(11) Zhao, S.; Liu, H.-X.; Qiu, Y.; Liu, S.-Q.; Diao, J.-X.; Chang, C.-R.; Si, R.; Guo, X.-H. An oxygen vacancy-rich two-dimensional Au/TiO_2 hybrid for synergistically enhanced electrochemical N_2 activation and reduction. J. Mater. Chem. A. 2020, 8 (14), 6586-6596. DOI: 10.1039/D0TA00658K.

(12) Chu, K.; Cheng, Y.-h.; Li, Q.-q.; Liu, Y.-p.; Tian, Y. Fe-doping induced morphological changes, oxygen vacancies and Ce^{3+}–Ce^{3+} pairs in CeO_2 for promoting electrocatalytic nitrogen fixation. J. Mater. Chem. A. 2020, 8 (12), 5865-5873. DOI: 10.1039/C9TA14260F.

(13) Akter, R.; Shah, S. S.; Ehsan, M. A.; Shaikh, M. N.; Zahir, M. H.; Aziz, M. A.; Ahammad, A. S. Transition-metal-based Catalysts for Electrochemical Synthesis of Ammonia by Nitrogen Reduction Reaction: Advancing the Green Ammonia Economy. Chem Asian J. 2024, 19 (16). DOI: 10.1002/asia.202300797.

(14) Zhao, L.; Zhao, J.; Zhao, J.; Zhang, L.; Wu, D.; Wang, H.; Li, J.; Ren, X.; Wei, Q. Artificial N_2 fixation to NH_3 by electrocatalytic Ru NPs at low overpotential. Nanotechnology 2020, 31 (29). DOI: 10.1088/1361-6528/ab814e.

(15) Skúlason, E.; Bligaard, T.; Gudmundsdóttir, S.; Studt, F.; Rossmeisl, J.; Abild-Pedersen, F.; Vegge, T.; Jónsson, H.; Nørskov, J. K. A theoretical evaluation of possible transition metal electro-catalysts for N_2 reduction. Phys. Chem. Chem. Phys. 2012, 14 (3), 1235-1245. DOI: 10.1039/C1CP22271F.

(16) Cook, R. L.; Sammells, A. F. Ambient temperature gas phase electrochemical nitrogen reduction to ammonia at ruthenium/solid polymer electrolyte interface. Catal. Lett. 1988, 1, 345-349. DOI: 10.1007/BF00766163.

(17) Chen, G.; Ding, M.; Zhang, K.; Shen, Z.; Wang, Y.; Ma, J.; Wang, A.; Li, Y.; Xu, H. Single-atomic ruthenium active sites on Ti_3C_2 MXene with oxygen-terminated surface synchronize enhanced activity and selectivity for electrocatalytic nitrogen reduction to ammonia. ChemSusChem 2022, 15 (3). DOI: 10.1002/cssc.202102352.

(18) Tao, H.; Choi, C.; Ding, L.-X.; Jiang, Z.; Han, Z.; Jia, M.; Fan, Q.; Gao, Y.; Wang, H.; Robertson, A. W.; et al. Nitrogen fixation by Ru single-atom electrocatalytic reduction. Chem 2019, 5 (1), 204-214. DOI: 10.1016/j.chempr.2018.10.007.

(19) Chen, Y.; Xu, R.; Li, Y.; Cai, L.; Yang, Y.; Zheng, Y.; Zuo, C.; Huang, H.; Wen, Z.; Wang, Q. Facile preparation of single-atom Ru catalysts via a two-dimensional interface directed synthesis technique for the NRR. Chem. Commun. 2023, 59 (36), 5403-5406. DOI: 10.1039/D3CC00721A.

(20) Zhao, R.; Liu, C.; Zhang, X.; Zhu, X.; Wei, P.; Ji, L.; Guo, Y.; Gao, S.; Luo, Y.; Wang, Z.; et al. An ultrasmall Ru_2P nanoparticles–reduced graphene oxide hybrid: an efficient electrocatalyst for NH_3 synthesis under ambient conditions. J. Mater. Chem. A. 2020, 8 (1), 77-81. DOI: 10.1039/C9TA10346E.

(21) Han, Z.; Huang, S.; Zhang, J.; Wang, F.; Han, S.; Wu, P.; He, M.; Zhuang, X. Single $Ru–N_4$ site-embedded porous carbons for electrocatalytic nitrogen reduction. ACS Appl. Mater. Interfaces 2023, 15 (10), 13025-13032. DOI: 10.1021/acsami.2c21744.

(22) Jia, H.-L.; Guo, C.-L.; Chen, R.-X.; Zhao, J.; Liu, R.; Guan, M.-Y. Ruthenium nanoparticles supported on S-doped graphene as an efficient HER electrocatalyst. New J. Chem. 2021, 45 (47), 22378-22385. DOI: 10.1039/D1NJ04765E.

(23) Over, H. Surface chemistry of ruthenium dioxide in heterogeneous catalysis and electrocatalysis: from fundamental to applied research. Chem. Rev. 2012, 112 (6), 3356-3426. DOI: 10.1021/cr200247n.

(24) Wang, J.; Zhang, L.; Wang, L.; Lei, W.; Wu, Z. S. Two-dimensional boron nitride for electronics and energy applications. Energy Environ. Mater. 2022, 5 (1), 10-44. DOI: 10.1002/eem2.12159.

(25) Ma, C.; Zhang, Y.; Yan, S.; Liu, B. Carbon-doped boron nitride nanosheets: A high-efficient electrocatalyst for ambient nitrogen reduction. Appl. Catal., B 2022, 315, 121574. DOI: 10.1016/j.apcatb.2022.121574.

(26) Salah, A.; Ren, H.-D.; Al-Ansi, N.; Tan, H.; Yu, F.; Yanchun, L.; Thamer, B. M.; Al-Salihy, A.; Zhao, L.; Li, Y. Dispersing small Ru nanoparticles into boron nitride remodified by reduced graphene oxide for high-efficient electrocatalytic hydrogen evolution reaction. J. Colloid Interface Sci. 2023, 644, 378-387. DOI: 10.1016/j.jcis.2023.04.094.

(27) Li, L. H.; Cervenka, J.; Watanabe, K.; Taniguchi, T.; Chen, Y. Strong oxidation resistance of atomically thin boron nitride nanosheets. ACS Nano 2014, 8 (2), 1457-1462. DOI: 10.1021/nn500059s.

(28) Sharma, M.; Sasaki, K.; Halada, G.; Pamula, K.; Kim, T.; Wong, S. S. Ketjenblack-Supported and Unsupported $ZrO_2–ZrN$ Nanoparticle Systems for Enabling Efficient Electrochemical

Nitrogen Reduction to Ammonia. ACS Appl. Mater. Interfaces 2025, 17, 1153–1166. DOI: 10.1021/acsami.4c17137.

(29) Liu, Z.; Zhang, M.; Wang, H.; Cang, D.; Ji, X.; Liu, B.; Yang, W.; Li, D.; Liu, J. Defective carbon-doped boron nitride nanosheets for highly efficient electrocatalytic conversion of N_2 to NH_3. ACS Sustainable Chem. Eng. 2020, 8 (13), 5278-5286. DOI: 10.1021/acssuschemeng.0c00330.

(30) Dong, S.; Xia, J.; Zhu, H.; Du, X.; Gu, Y.; Liu, Q.; Luo, Y.; Kong, Q.; Guo, H.; Li, T. ZrO_2/C Nanosphere Enables High-Efficiency Nitrogen Reduction to Ammonia at Ambient Conditions. ChemCatChem 2022, 14 (17). DOI: 10.1002/cctc.202200458.

(31) Zhang, Y.; Du, H.; Ma, Y.; Ji, L.; Guo, H.; Tian, Z.; Chen, H.; Huang, H.; Cui, G.; Asiri, A. M. Hexagonal boron nitride nanosheet for effective ambient N_2 fixation to NH_3. Nano Res. 2019, 12, 919-924. DOI: 10.1007/s12274-019-2323-x.

(32) Watt, G. W.; Chrisp, J. D. Spectrophotometric method for determination of hydrazine. Anal. Chem. 1952, 24 (12), 2006-2008. DOI: 10.1021/ac60072a044.

(33) Shehzad, A.; Yi, Q.; Luo, Z.; Cui, C. Electrocatalytic Nitrogen Reduction to Ammonia by Graphene-Supported Au_4Cu_2 and Au_2Ag_2 Nanoclusters. Nanoscale 2025, 17, 7453-7459. DOI: 10.1039/D4NR05341A.

(34) Yao, Y.; Wang, H.; Yuan, X.-z.; Li, H.; Shao, M. Electrochemical Nitrogen Reduction Reaction on Ruthenium. ACS Energy Lett. 2019, 4 (6), 1336–1341. DOI: 10.1021/acsenergylett.9b00699.

(35) Zhu, Y.; Klingenhof, M.; Gao, C.; Koketsu, T.; Weiser, G.; Pi, Y.; Liu, S.; Sui, L.; Hou, J.; Li, J.; et al. Facilitating alkaline hydrogen evolution reaction on the hetero-interfaced Ru/RuO_2 through Pt single atoms doping. Nat. Commun. 2024, 15 (1), 1447. DOI: 10.1038/s41467-024-45654-9.

(36) Haque, A.; Narayan, J. Conversion of h-BN into c-BN for tuning optoelectronic properties. Mater. Adv. 2020, 1 (4), 830-836. DOI: 10.1039/d0ma00008f.

(37) Jo, H.-G.; Kim, K.-H.; Ahn, H.-J. Well-dispersed Pt/RuO_2-decorated mesoporous N-doped carbon as a hybrid electrocatalyst for Li–O_2 batteries. RSC Adv. 2021, 11 (20), 12209-12217. DOI: 10.1039/d1ra00740h.

(38) Zhou, L.; Shao, Y.; Yin, F.; Li, J.; Kang, F.; Lv, R. Stabilizing non-iridium active sites by non-stoichiometric oxide for acidic water oxidation at high current density. Nat. Commun. 2023, 14 (1), 7644. DOI: 10.1038/s41467-023-43466-x.

(39) Wang, Z.; Priego, P.; Meziani, M. J.; Wirth, K.; Bhattacharya, S.; Rao, A.; Wang, P.; Sun, Y.-P. Dispersion of high-quality boron nitride nanosheets in polyethylene for nanocomposites of superior thermal transport properties. Nanoscale Adv. 2020, 2 (6), 2507-2513. DOI: 10.1039/d0na00190b.

(40) Türkez, H.; Arslan, M. E.; Sönmez, E.; Açikyildiz, M.; Tatar, A.; Geyikoğlu, F. Synthesis, characterization and cytotoxicity of boron nitride nanoparticles: emphasis on toxicogenomics. Cytotechnology 2019, 71, 351-361. DOI: 10.1007/s10616-019-00292-8.

(41) Huang, Z.; He, G.; Li, J.; Wang, F.; Zhang, R.; Yao, D. Exponentially reduced carrier mobility of natural ester via blocking effect of 2D hexagonal boron nitride nanosheets. High Volt. 2021, 6 (2), 219-229. DOI: 10.1049/hve2.12017.

(42) Xiong, Y.; Xiong, C.; Wei, S.; Yang, H.; Mai, Y.; Xu, W.; Yang, S.; Dai, G.; Song, S.; Xiong, J.; et al. Study on the bonding state for carbon–boron nitrogen with different ball milling time. Appl. Surf. Sci. 2006, 253 (5), 2515-2521. DOI: 10.1016/j.apsusc.2006.05.009.

(43) Wibbelt, M.; Kohl, H.; Kohler-Redlich, P. Multiple-scattering calculations of electron-energy-loss near-edge structures of existing and predicted phases in the ternary system BCN. Phys. Rev. B 1999, 59 (18), 11739. DOI: 10.1103/PhysRevB.59.11739.

(44) Maquin, B.; Derré, A.; Labrugère, C.; Trinquecoste, M.; Chadeyron, P.; Delhaès, P. Submicronic powders containing carbon, boron and nitrogen: their preparation by chemical vapour deposition and their characterization. Carbon 2000, 38 (1), 145-156. DOI: 10.1016/S0008-6223(99)00102-5.

(45) Bavand, R.; Yelon, A.; Sacher, E. X-ray photoelectron spectroscopic and morphologic studies of Ru nanoparticles deposited onto highly oriented pyrolytic graphite. Appl. Surf. Sci. 2015, 355, 279-289. DOI: 10.1016/j.apsusc.2015.06.202.

(46) Morgan, D. J. Resolving ruthenium: XPS studies of common ruthenium materials. Surf. Interface Anal. 2015, 47 (11), 1072-1079. DOI: 10.1002/sia.5852.

(47) Diulus, J. T.; Tobler, B.; Osterwalder, J.; Novotny, Z. Thermal oxidation of Ru (0001) to RuO_2 (110) studied with ambient pressure x-ray photoelectron spectroscopy. J. Phys. D: Appl. Phys. 2021, 54 (24), 244001. DOI: 10.1088/1361-6463/abedfd.

(48) Devadas, A.; Baranton, S.; Coutanceau, C. Green synthesis and modification of RuO_2 materials for the oxygen evolution reaction. Front. Energy Res. 2020, 8, 571704. DOI: 10.3389/fenrg.2020.571704.

(49) Haque, A.; Taqy, S.; Narayan, J. Recent progress in cubic boron nitride (c-bn) fabrication by pulsed laser annealing for optoelectronic applications. J. Electron. Mater. 2024, 53 (8), 4308-4340. DOI: 10.1007/s11664-024-11171-0.

(50) Urbansky, E. T. Perchlorate chemistry: implications for analysis and remediation. Biorem. J. 1998, 2 (2), 81-95.

(51) Qiu, W.; Xie, X.-Y.; Qiu, J.; Fang, W.-H.; Liang, R.; Ren, X.; Ji, X.; Cui, G.; Asiri, A. M.; Cui, G.; et al. High-performance artificial nitrogen fixation at ambient conditions using a metal-free electrocatalyst. Nat. Commun. 2018, 9 (1), 3485. DOI: 10.1038/s41467-018-05758-5.

(52) Biswas, A.; Ghosh, B.; Dey, R. S. Refining the spectroscopic detection technique: A pivot in the electrochemical ammonia synthesis. Langmuir 2023, 39 (10), 3810-3820. DOI: 10.1021/acs.langmuir.3c00201.

(53) Yang, J.; Qi, H.; Li, A.; Liu, X.; Yang, X.; Zhang, S.; Zhao, Q.; Jiang, Q.; Su, Y.; Zhang, L.; et al. Potential-driven restructuring of Cu single atoms to nanoparticles for boosting the electrochemical reduction of nitrate to ammonia. J. Am. Chem. Soc. 2022, 144 (27), 12062-12071. DOI: 10.1021/jacs.2c02262.

(54) Cui, M.; Zhang, T.; Wang, M.; Xu, W.; Zhang, Y.; Song, P.; Wang, C.; Yang, Y.; Zhang, X.; Fan, X. Chemically anchoring molybdenum atoms onto micropore-rich VN nanosheet for boosted nitrogen electro-fixation via hydrogen bonds. Chem. Eng. J. 2022, 446, 136915. DOI: 10.1016/j.cej.2022.136915.

(55) Cheng, S.; Gao, Y.-J.; Yan, Y.-L.; Gao, X.; Zhang, S.-H.; Zhuang, G.-L.; Deng, S.-W.; Wei, Z.-Z.; Zhong, X.; Wang, J.-G. Oxygen vacancy enhancing mechanism of nitrogen reduction reaction property in Ru/TiO_2. J. Energy Chem. 2019, 39, 144-151. DOI: 10.1016/j.jechem.2019.01.020.

(56) Sun, W.; Sahin, N. E.; Sun, D.; Wu, X.; Munoz, C.; Thakare, J.; Aulich, T.; Zhang, J.; Hou, X.; Oncel, N.; et al. One-pot synthesis of ruthenium-based nanocatalyst using reduced graphene oxide as matrix for electrochemical synthesis of ammonia. ACS Appl. Mater. Interfaces 2022, 15 (1), 1115-1128. DOI: 10.1021/acsami.2c18413.

(57) Wang, H.; Li, Y.; Li, C.; Deng, K.; Wang, Z.; Xu, Y.; Li, X.; Xue, H.; Wang, L. One-pot synthesis of bi-metallic PdRu tripods as an efficient catalyst for electrocatalytic nitrogen reduction to ammonia. J. Mater. Chem. A. 2019, 7 (2), 801-805. DOI: 10.1039/C8TA09482A.

(58) Wang, H.; Li, Y.; Yang, D.; Qian, X.; Wang, Z.; Xu, Y.; Li, X.; Xue, H.; Wang, L. Direct fabrication of bi-metallic PdRu nanorod assemblies for electrochemical ammonia synthesis. Nanoscale 2019, 11 (12), 5499-5505. DOI: 10.1039/C8NR10398D.

(59) Chalkley, M. J.; Drover, M. W.; Peters, J. C. Catalytic N_2-to-NH_3 (or-N_2H_4) conversion by well-defined molecular coordination complexes. Chem. Rev. 2020, 120 (12), 5582-5636. DOI: 10.1021/acs.chemrev.9b00638.

(60) Wu, J.; Wang, S.; Ji, R.; Kai, D.; Kong, J.; Liu, S.; Thitsartarn, W.; Tan, B. H.; Chua, M. H.; Xu, J.; et al. In situ characterization techniques for electrochemical nitrogen reduction reaction. ACS Nano 2024, 18 (32), 20934-20956. DOI: 10.1021/acsnano.4c05956.

(61) Liu, R.; Fei, H.; Wang, J.; Guo, T.; Liu, F.; Wu, Z.; Wang, D. Unveiling the synergistic effect between the metallic phase and bridging S species over MoS_2 for highly efficient nitrogen fixation. Appl. Catal., B 2024, 343, 123469. DOI: 10.1016/j.apcatb.2023.123469.

(62) Long, X.; Huang, F.; Yao, Z.; Li, P.; Zhong, T.; Zhao, H.; Tian, S.; Shu, D.; He, C. Advancements in Electrocatalytic Nitrogen Reduction: A Comprehensive Review of Single-Atom Catalysts for Sustainable Ammonia Synthesis. Small 2024, 20 (32), 2400551. DOI: 10.1002/smll.202400551.

(63) Dang, Y.; Wu, T.; Tan, H.; Wang, J.; Cui, C.; Kerns, P.; Zhao, W.; Posada, L.; Wen, L.; Suib, S. L. Partially reduced Ru/RuO_2 composites as efficient and pH-universal electrocatalysts for hydrogen evolution. Energy Environ. Sci. 2021, 14 (10), 5433-5443. DOI: 10.1039/D1EE02380B.

(64) Yang, P.; Li, Q.; Wang, Z.; Gao, Y.; Jin, W.; Xiao, W.; Wang, L.; Liu, F.; Wu, Z. Lanthanum and tungsten co-doped ruthenium dioxide for fresh/sea-water alkaline hydrogen evolution reaction. Scr. Mater. 2024, 240, 115849. DOI: 10.1016/j.scriptamat.2023.115849.

(65) Wang, D.; Azofra, L. M.; Harb, M.; Cavallo, L.; Zhang, X.; Suryanto, B. H.; MacFarlane, D. R. Energy-efficient nitrogen reduction to ammonia at low overpotential in aqueous electrolyte under ambient conditions. ChemSusChem 2018, 11 (19), 3416-3422. DOI: 10.1002/cssc.201801632.

(66) Ju, H.; Seo, D. H.; Chung, S.; Mao, X.; An, B.-S.; Musameh, M.; Gengenbach, T. R.; Shon, H.; Du, A.; Bendavid, A.; et al. Green ammonia synthesis using CeO_2/RuO_2 nanolayers on vertical graphene catalyst via electrochemical route in alkaline electrolyte. Nanoscale 2022, 14 (4), 1395-1408. DOI: 10.1039/D1NR06411H.

(67) Li, L.; Jiang, Y.-F.; Zhang, T.; Cai, H.; Zhou, Y.; Lin, B.; Lin, X.; Zheng, Y.; Zheng, L.; Wang, X. Size sensitivity of supported Ru catalysts for ammonia synthesis: From nanoparticles to subnanometric clusters and atomic clusters. Chem 2022, 8 (3), 749-768. DOI: 10.1016/j.chempr.2021.11.008.

(68) Kim, Y. D.; Seitsonen, A. P.; Over, H. Adsorption Characteristics of CO and N_2 on RuO_2 (110). Phys. Rev. B 2001, 63 (11), 115419. DOI: 10.1103/PhysRevB.63.115419.

(69) Wang, Y.; Jacobi, K.; Schöne, W.-D.; Ertl, G. Catalytic oxidation of ammonia on RuO_2 (110) surfaces: mechanism and selectivity. J. Phys. Chem. B 2005, 109 (16), 7883-7893. DOI: 10.1021/jp045735v.

(70) de Araujo, R. G.; Perez, J. Nitrogen Electrochemical Reduction Reaction Pathways Evidenced by Online Electrochemical Mass Spectrometry and Isotope Labeling on the MoS_2 Surface. ACS Electrochem. 2025, 1 (3), 294-302. DOI: 10.1021/acselectrochem.4c00135.

Table of Contents graphic:

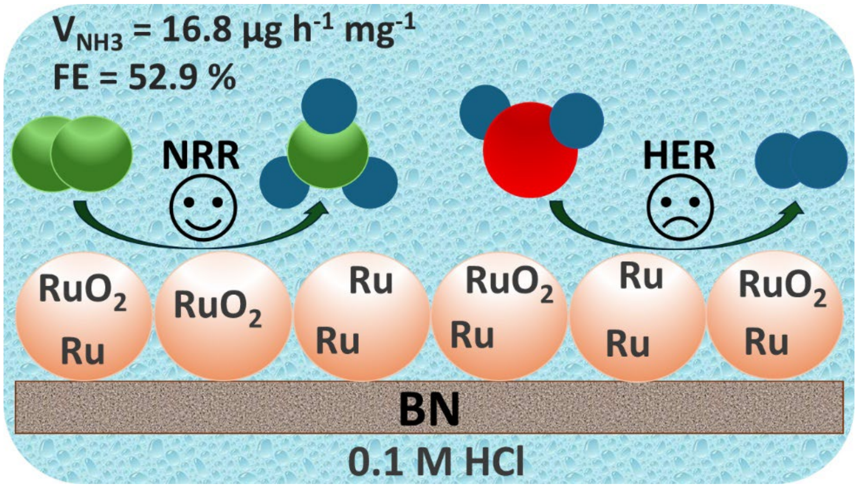

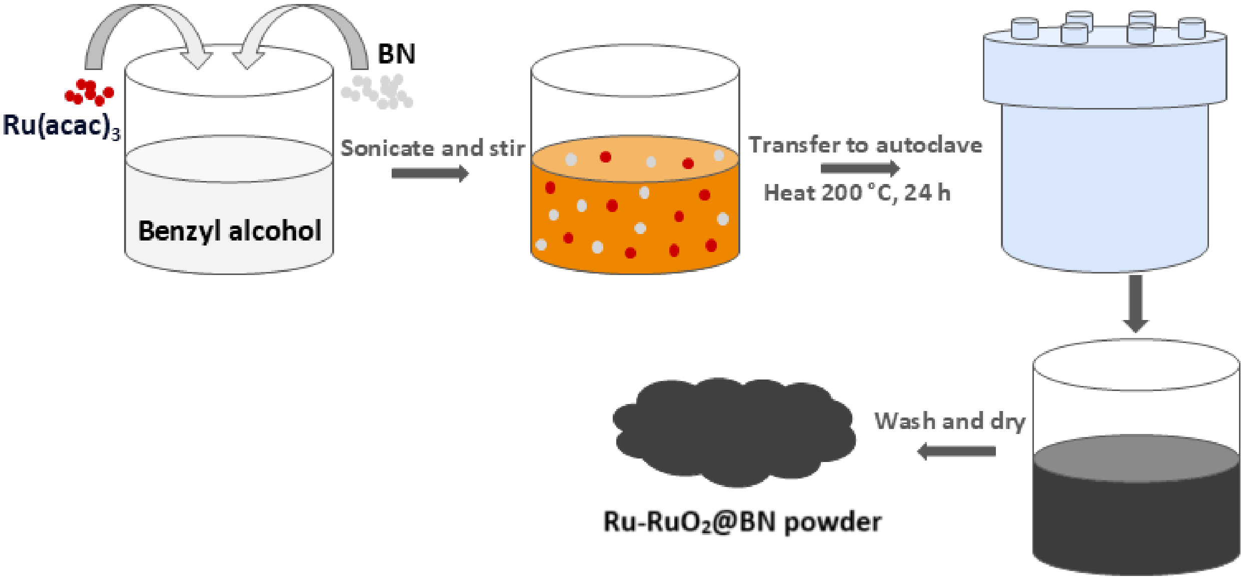

Figure 1. Schematic stepwise illustration for the synthesis of Ru-RuO$_2$@BN.

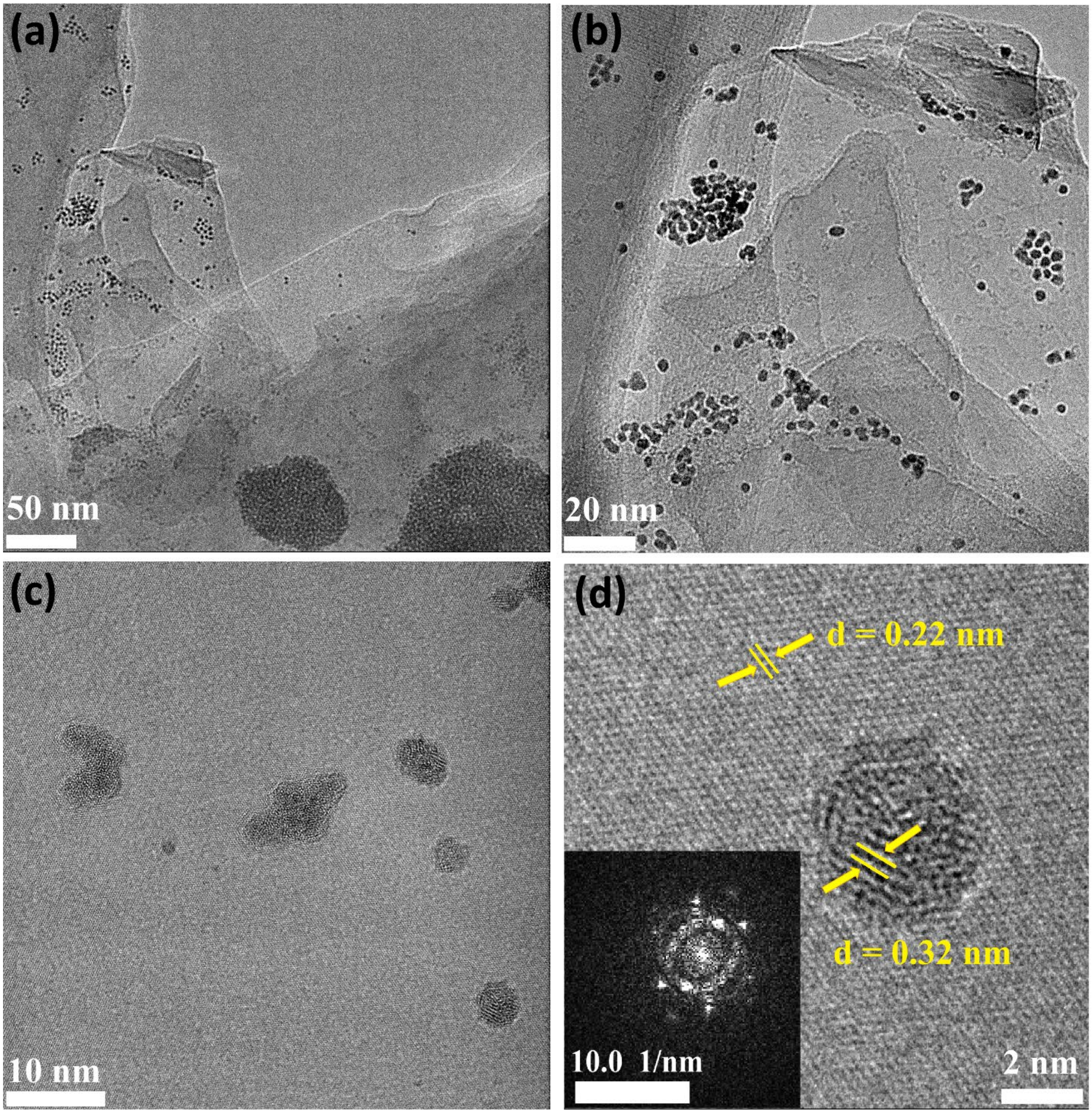

Figure 2. (a-c) TEM images of Ru-RuO_2@BN, along with HRTEM with the inset highlighting the corresponding electron diffraction pattern. (d) Lattice fringes are visible with *d* spacings of 0.32 nm and 0.22 nm, ascribed to the (110) plane of RuO_2 and the (100) plane of BN, respectively.

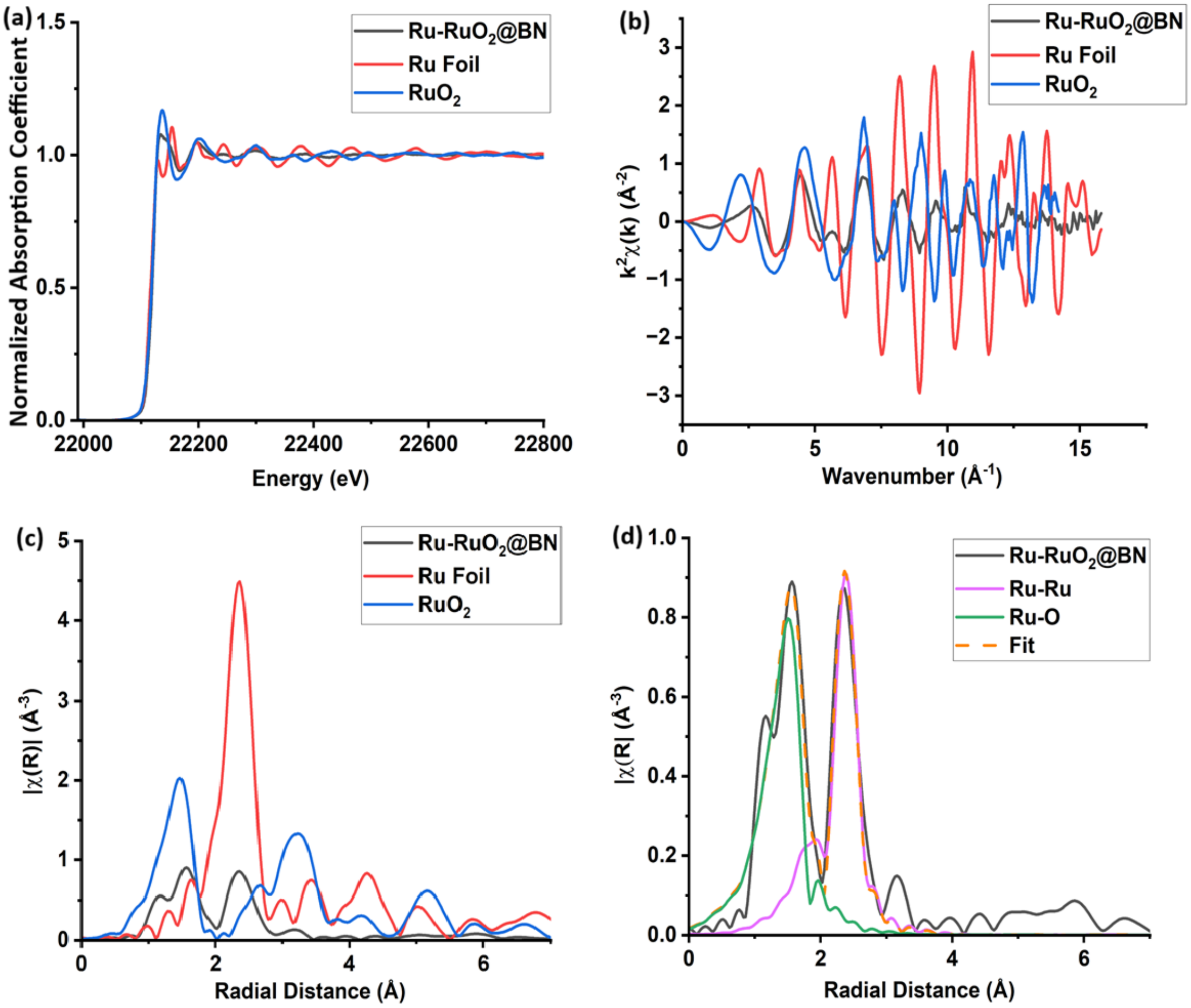

Figure 3. X-ray absorption coefficient at Ru K-edge for Ru-RuO2@BN, Ru (metal) reference and RuO2 reference in (a) normalized energy space, (b) k-space, and (c) r-space. The presence of isosbestic points is an indication that the Ru-RuO2@BN sample maintains co-existing Ru metal and Ru oxide phases. In the r-space plot, the first peak corresponds to Ru-O and the second is associated with Ru-Ru (metal) contributions. (d) Ru K-edge EXAFS data and fit for Ru-RuO2@BN in r-space.

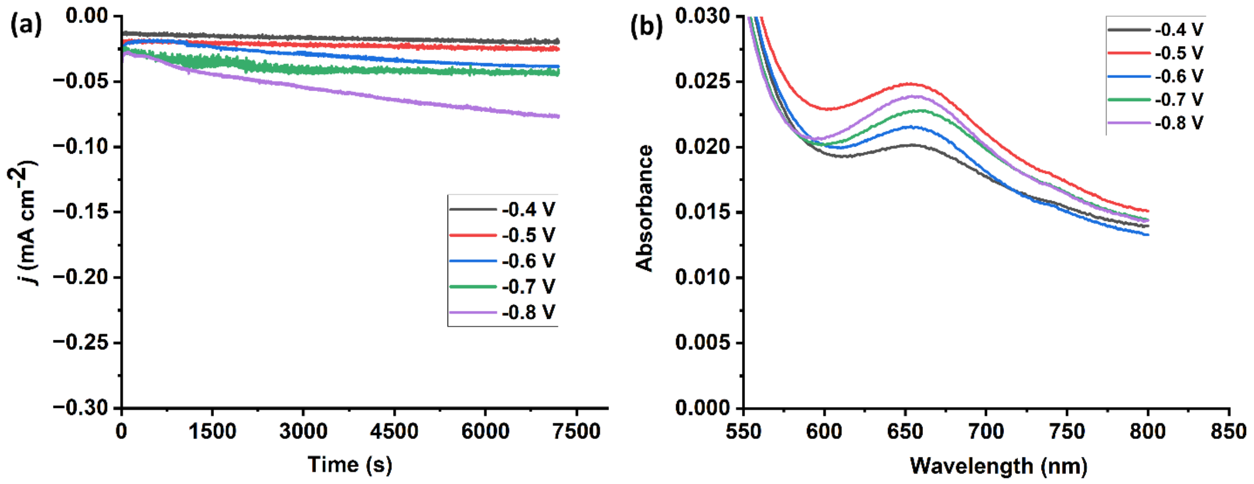

Figure 4. (a) Chronoamperometry results associated with C- Ru-RuO$_2$@BN, collected at various potentials. (b) UV−visible absorption curves of the electrolytes using the indophenol method are shown after 2 h of electrolysis, measured against different potentials.

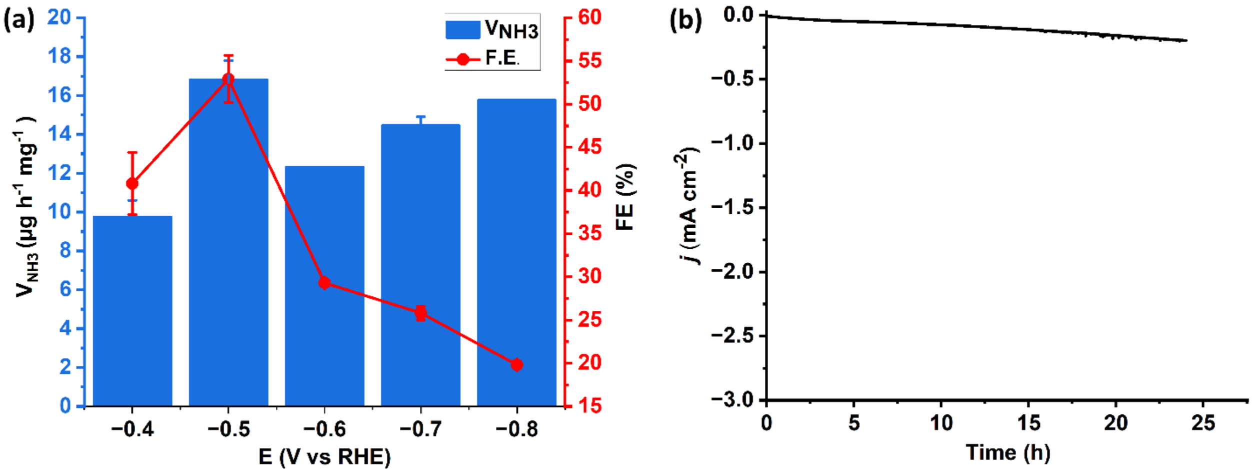

Figure 5. (a) V$_{NH3}$ and FE data for C-Ru-RuO$_2$@BN at each given potential. (b) Complementary chronoamperometry data were collected on C- Ru-RuO$_2$@BN, measured at −0.5 V for 24 h.

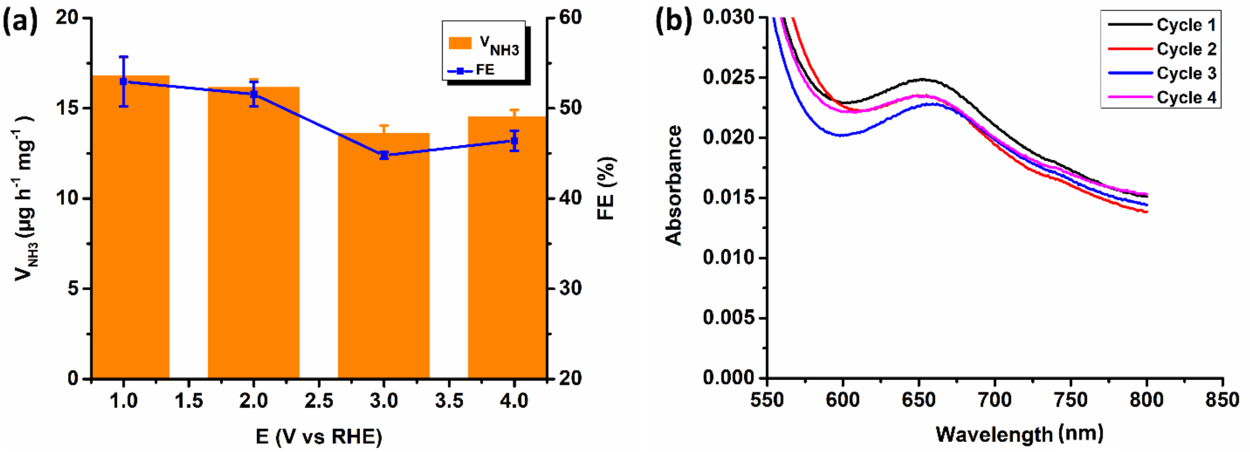

Figure 6. (a) Recycling test of C- Ru-RuO2@BN at −0.5 V and (b) the corresponding UV−visible absorption curves for cycles 1 to 4.

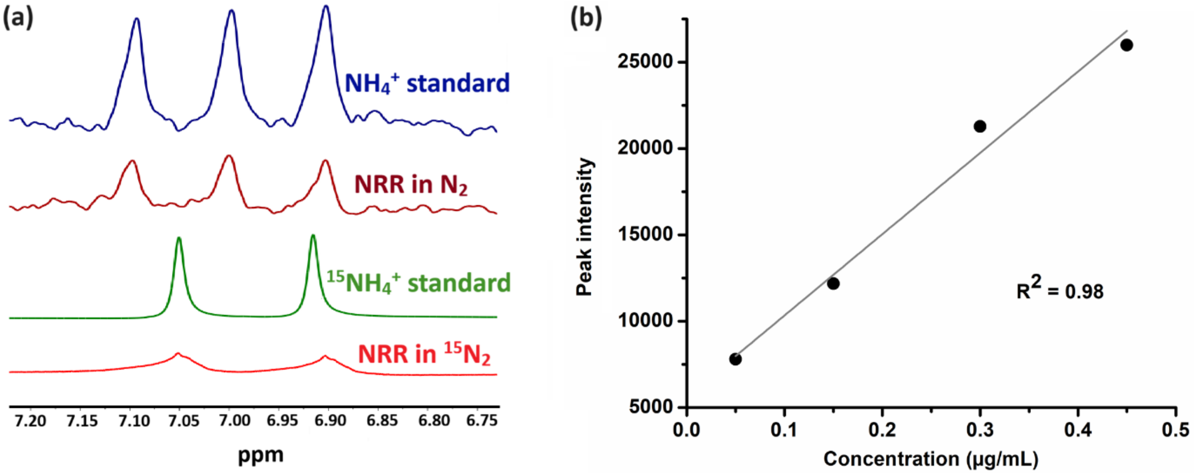

Figure 7. (a) ^{1}H NMR spectra (500 MHz) of NH_4^+, including NH_4^+ standard samples with concentrations of 0.45 μg mL^{-1} (blue curve), NRR samples after electrolysis at −0.5 V vs RHE using N_2 as the feeding gas (maroon curve), $^{15}NH_4^+$ standard samples with a concentration of 0.45 μg mL^{-1} (green curve), and NRR samples after electrolysis at −0.5 V vs RHE using $^{15}N_2$ as the feeding gas (red curve), respectively. **(b)** The calibration curve of the ^{1}H NMR signal at 6.99 ppm is given, using standard solutions of varying concentrations of NH_4^+.

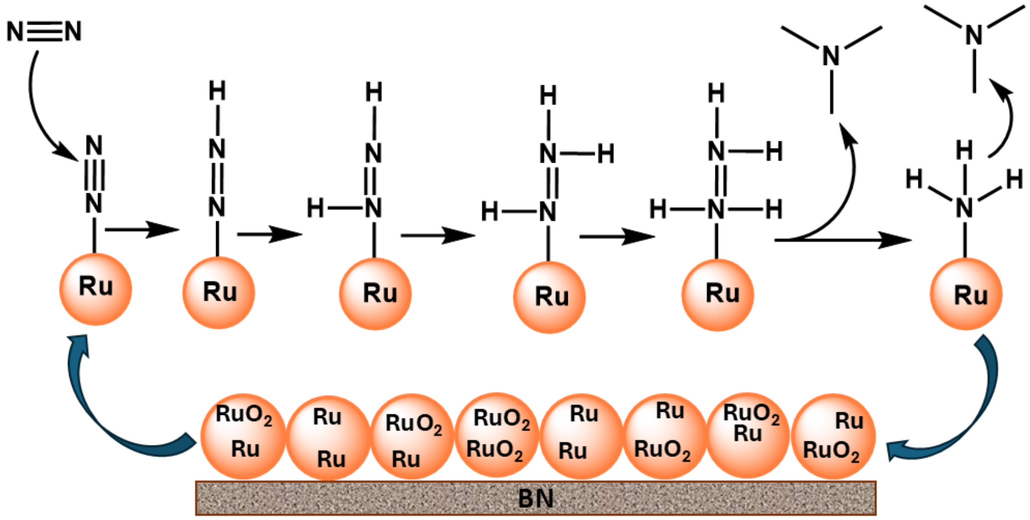

Figure 8. Proposed mechanism of possible electrochemical pathways for NRR on an Ru-RuO_2@BN electrocatalyst surface.

Table 1. Data used for calculating V_{NH3} and FE values for Ru-RuO_2@BN are provided to at most 3 significant digits. Error bars have also been added in, based on 3-5 replicate experimental runs performed at each potential.

E (V vs RHE)	Absorbance at ≈ 655 nm	$[NH_3]$ (μg/mL)	V_{NH3} (μg h^{-1} mg^{-1})	Q (mA•s)	FE (%)
-0.4	0.020	0.07	9.75 ± 0.85	121.9	40.8 ± 3.60
-0.5	0.025	0.13	16.8 ± 1.0	160.2	52.9 ± 2.75
-0.6	0.022	0.09	12.3 ± 0.005	215.8	29.3 ± 0.01
-0.7	0.023	0.11	14.45 ± 0.45	286.3	25.8 ± 0.78
-0.8	0.024	0.12	15.75 ± 0.005	4.7.7	19.8 ± 0.01

The volume of electrolyte used in all experiments was 40 mL, and the electrolysis time was 2 h.